Normalized difference chlorophyll index: A novel model for remote estimation of chlorophyll-*a* concentration in turbid productive waters

Sachidananda Mishra [a], Deepak R. Mishra [a,b,*]

[a] Department of Geosciences and Geosystems Research Institute, Mississippi State University, United States
[b] Northern Gulf Institute, Mississippi State University, United States

ARTICLE INFO

ABSTRACT

We propose a normalized difference chlorophyll index (NDCI) to predict chlorophyll-a (chl-*a*) concentration from remote sensing data in estuarine and coastal turbid productive (case 2) waters. NDCI calibration and validation results derived from simulated and MEdium Resolution Imaging Spectrometer (MERIS) datasets show its potential application to widely varying water types and geographic regions. A quadratic function ($R^2 = 0.95$, $p < 0.0001$) accurately explained the variance in the simulated data for a chl-*a* range of 1–60 mg m^{-3}. Similarly a twofold calibration and validation of chl-*a* models using MERIS dataset, (chl-*a* range: 0.9–28.1 mg m^{-3}) yielded R^2 of 0.9, and RMSE of ~2 mg m^{-3} respectively. NDCI was applied on images over the Chesapeake Bay and Delaware Bay, the Mobile Bay, and the Mississippi River delta region in the northern Gulf of Mexico. The newly developed algorithm was successful in predicting chl-*a* concentration with approximately 12% overall bias for all above study regions. Findings from this research imply that NDCI can be successfully used on MERIS images to quantitatively monitor chl-*a* in inland coastal and estuarine waters. In case of remote coastal waters with no ground truth data, NDCI can be used to detect algal bloom and qualitatively infer chl-*a* concentration ranges very similar to NDVI's application in terrestrial vegetation studies.

1. Introduction

Accurate remote estimation of biophysical parameters such as chlorophyll-*a* (chl-*a*) and phytoplankton biomass in turbid productive waters is essential for large-scale and multi-temporal studies related to primary production, carbon cycle, biogeochemical cycles, and overall inland and coastal water quality. However, it is still a challenge because of the presence of non-covarying optically active constituents whose absorption features overlap with chl-*a*. Spectral channels in the blue-green part of the electromagnetic spectrum are heavily affected by the presence of constituents such as Colored Dissolved Organic Matter (CDOM), detritus, and tripton. Empirical algorithms (e.g., OC4v4) that use blue and green spectral channels often provide a relatively accurate estimate of chl-*a* in case 1 waters where the total non-water absorption is dominated by phytoplankton, however, do not provide reasonable estimates of chl-*a* in turbid productive waters (O'Reilly et al., 1998). In order to reduce the estimation error of chl-*a* in turbid productive waters, semi-analytical models have also been proposed (Gons et al., 2002; Maritorena et al., 2002). However, the success of these semi-analytical models depends on the accurate parameterization of the inherent optical properties of the medium that often poses a considerable challenge. Magnuson et al. (2004) re-parameterized the original semi-

analytical model proposed by Maritorena et al. (2002) to make it suitable for the Chesapeake Bay and Mid-Atlantic Bight region. They reported that the re-parameterized model was successful in attributing CDOM absorption in the total absorption budget and offered accurate estimation when compared to OC4v4 model and the accuracy of chl-*a* estimation was within 30–50% of the in situ measured values. Even though the re-parameterized semi analytical model produced better accuracy than OC4v4, the uncertainty was still very high. Because of the difficulties in obtaining the information for re-parameterization, such as specific absorption coefficient of phytoplankton, $a_{ph}*(\lambda)$, spectral slope of colored dissolved organic matter, S_{CDOM}, and spectral slope of detritus, $S_{detritus}$, alternative approaches have been encouraged to improve chl-*a* estimation in turbid productive waters. Over the past years numerous algorithms have been proposed to quantify chl-*a* in turbid productive waters using red-near infrared (NIR) bands and these algorithms can be classified into three primary groups such as 1) two-band empirical (Moses et al., 2009; Tzortziou et al., 2007), 2) three or four-band empirical (Dall'Olmo & Gitelson, 2005; Le et al., 2009), and 3) three-band semi-analytical (Gons, 1999; Gons et al., 2002) models. In this study, we have assessed the accuracy of red and NIR based empirical and semi-analytical algorithms in geographically diverse water bodies and propose a novel band difference algorithm for accurately mapping chl-*a* concentration in turbid productive waters.

We have selected four algorithms from the list above for further validation and examination of their performance and transferability to different water bodies. The selected algorithms discussed below are widely applied and unique in their band architecture.

* Corresponding author at: Department of Geosciences, Mississippi State University, P.O. Box 5448, Mississippi State, MS 39762-5448, United States. Tel.: +1 662 268 1032x233; fax: +1 662 325 9423.
E-mail address: dmishra@gri.msstate.edu (D. Mishra).

Moses et al. (2009) presented a two-band model (hereafter M09) using red and NIR bands to quantify chl-*a* in turbid productive waters. To match the band configuration of MERIS sensor, the conceptual model was designed as:

$$C_{chl-a} \propto R_{rs}^{-1}(665) \times R_{rs}(708) \tag{1}$$

They applied M09 on MERIS images over Azov Sea, Russia and reported the high accuracy potential of the model to estimate chl-*a* in turbid productive waters. Similarly, Tzortziou et al. (2007) collected an extensive bio-optical dataset to examine the relationship between inherent and apparent optical properties in the mid Chesapeake Bay, USA. They observed a better relationship ($R^2 = 0.54$) between remote sensing reflectance (R_{rs}) ratio at 677 and 554 nm, $R_{rs}(677)/R_{rs}(554)$, and chl-*a* concentration in the bay compared to blue-green spectral band ratios. In this study we have modified this ratio based on the MERIS band configuration, $R_{rs}(665)/R_{rs}(559)$ and named it T07 for further reference.

$$C_{chl-a} \propto R_{rs}^{-1}(559) \times R_{rs}(665) \tag{2}$$

Dall'Olmo and Gitelson (2005) (hereafter D05) presented a three-band model using red and NIR bands. The three-band model architecture was as follows:

$$C_{chl-a} \propto \left[R_{rs}^{-1}(665) - R_{rs}^{-1}(708) \right] \times R_{rs}(753) \tag{3}$$

The three band algorithm was based on several assumptions including, (i) the absorption by suspended solids and CDOM beyond 700 nm is approximately equal to that at 665–675 nm and the difference between them is very small and can be neglected, (ii) the total chl-*a*, CDOM, and total suspended sediment (TSS) absorption beyond 730 nm is nearly zero, and (iii) back-scattering coefficient of chl-*a* is spectrally invariant. They reported that D05 was successful to predict accurate estimate of chl-*a* in turbid productive water bodies with wide range of optical complexity. Moses et al.(2009) further validated D05 using MERIS data from the Azov Sea and documented that D05 was able to retrieve chl-*a* concentration with a RMSE of 5.02 mg m^{-3} (for a chl-*a* range: 18.37–47.86 mg m^{-3}).

Gons et al. (2008) presented a semi-analytical algorithm (hereafter G08) for chl-*a* retrieval using MERIS data which was a modification of the parent algorithm (Gons, 1999). G08 uses the relationship between inherent optical properties and the R_{rs} at three wavelengths, solves for chl-*a* absorption at 665 nm, and estimates chl-*a* by dividing $a_{chl}(665)$ by the specific absorption coefficient of chl-*a*, $a_{chl-a}^*(665)$.

$$[Chl-a] = \left\{ \left[\frac{R_{rs}(708.75)}{R_{rs}(665)} \right] * (0.70 + b_b) - 0.40 - b_b^{1.06} \right\} / 0.016 \tag{4}$$

where b_b is the back-scattering coefficient and was expressed as:

$$b_b = \frac{1.61 * R_{rs}(775)}{0.082 - 0.6 * R_{rs}(775)}$$

Gons et al. (2008) reported that G08 successfully retrieved chl-*a* concentration in the Laurentian great lakes producing residuals less than 35% of the measured values. They also reported that G08 did not perform well in areas with chl-*a* less than 5 mg m^{-3} and even produced some negative values in oligotrophic waters.

Although, the three-band algorithms, D05 and G08, have excellent predictive ability, the biggest challenge of these models is that they require R_{rs} measurements at 753 and 775 nm. Based on existing atmospheric correction schemes for turbid productive waters, getting reliable estimates of R_{rs} at these wavelengths is a difficult task. In addition, another inherent difficulty of semi-analytical models such

as G08 is the use of $a_{chl-a}^*(665)$. Any uncertainty associated with $a_{chl-a}^*(665)$ can contribute to inaccurate estimates of chl-*a*.

After carefully examining the strengths and weaknesses of the above models, our goal in this research was to develop an algorithm that can perform better than the existing algorithms. Two of the most important criteria for a successful spectral algorithm development include (1) applicability to satellite data, and (2) transferability to widely varying geographic regions without producing significant uncertainties. We have tested and analyzed both criteria in this study as part of the model validation. We propose a novel index, Normalized Difference Chlorophyll Index (NDCI), and demonstrate its sensitivity to chl-*a* concentration in turbid productive waters. We have calibrated and validated a chl-*a* model using NDCI by analyzing four datasets (one simulated and three field datasets) representing unique turbid productive water bodies and presented its potential use for chl-*a* estimation in optically complex waters. The purpose of using a simulated data was to test the model performance and sensitivity to a wide range of optical parameters in the water.

NDCI uses R_{rs} at 665 nm, $R_{rs}(665)$, and 708 nm, $R_{rs}(708)$, emulating the Medium Resolution Imaging Spectrometer (MERIS) channels. Similar to other turbid productive chl-*a* algorithms, this index uses the information from the reflectance peak centered at 700 nm which is maximally sensitive to the variations in chl-*a* concentration in water. Similarly, a wide spectral absorption peak between 665 nm and 675 nm is generally assigned to the absorption by chl-*a* pigments. We selected the two spectral features centered at 665 nm and 708 nm to develop NDCI and to avoid the confounding influence of CDOM and TSS on the water reflectance spectra at shorter wavelengths. Also, as both bands are closely located, we assume that the CDOM and TSS absorption is similar in magnitude. Based on the results from bio-optical modeling in this study, the combined range of CDOM and TSS absorptions at 665 nm (0.0193–0.1899 m^{-1}) and 708 nm (0.015–0.1603 m^{-1}) in the study regions are approximately equal and the difference between them can be assumed as negligible. Further, following the simplistic concept of normalized difference vegetation index (NDVI) applied in vegetation status monitoring; NDCI was developed by taking the spectral band difference at 708 nm and 665 nm and normalizing by the sum of their reflectance to eliminate any uncertainties in the estimation of R_{rs}, seasonal solar azimuth differences, and atmospheric contributions at those wavelengths. NDCI is formulated as:

$$C_{chl-a} \propto \frac{[R_{rs}(708) - R_{rs}(665)]}{[R_{rs}(708) + R_{rs}(665)]} \tag{5}$$

The overarching objective of this research was to improve the accuracy of chl-*a* retrieval in turbid productive waters using a simple, easy to implement, intuitive (such as NDVI for vegetation), and universal model. Throughout this paper, we have tested these criteria using several steps including, (1) developing a dataset simulating a wide range of bio-optical parameters to examine the conceptual model, (2) testing the model using an in situ dataset collected from a global bio-optical data archive and corresponding MERIS data, (3) evaluating the performance of several existing chl-*a* algorithms for turbid productive waters using the simulated and remotely sensed datasets, (4) applying the model in three unique study regions, such as Chesapeake-Delaware Bay, the Mississippi River Delta, and the Mobile Bay, and (5) finally and most importantly, developing a generalized but practical relationship between NDCI values and chl-*a* range in an attempt to make NDCI intuitive and applicable when/where ground truth data is not available.

2. Data and methods

2.1. Bio-optical modeling

The simulated R_{rs} spectra used for the model conception, calibration, and validation were approximated by the following method.

Irradiance reflectance, $R(z,\lambda)$, is defined as (Morel & Prieur, 1977)

$$R(z, \lambda) = \frac{E_u(\lambda, z)}{E_d(\lambda, z)}, \tag{6}$$

where, $E_u(\lambda,z)$ and $E_d(\lambda,z)$ are upwelling irradiance (W m^{-2} nm^{-1}) and downwelling irradiance (W m^{-2} nm^{-1}) at depth (z) in the water column. Gordon et al. (1975) have approximated $R(0,\lambda)$ at the water surface as a function of the in-water absorption and scattering coefficients as:

$$R(0, \lambda) = f \frac{b_b(\lambda)}{a(\lambda) + b_b(\lambda)} \tag{7}$$

where, $b_b(\lambda)$ is the total backscattering coefficient (m^{-1}); $a(\lambda)$ is the total absorption coefficient (m^{-1}); and f is the proportionality factor that depends on the solar zenith angle and light field geometry. Further, Kirk (1984) modeled f as a function of the cosine of the solar zenith angle (μ_0) of the refracted photons as:

$$f(\mu_0) = -0.629\mu_0 + 0.975 \tag{8}$$

$R(0,\lambda)$ is closely related to the spectral remote sensing reflectance, $R_{rs}(\lambda)$ as (Carder & Steward, 1985):

$$R_{rs}(\lambda, 0) = \frac{L_w(\lambda, 0)}{E_d(\lambda, 0)} \tag{9}$$

where, $L_w(\lambda,0)$ is the water leaving radiance (W m^{-2} sr^{-1} nm^{-1}); and $E_d(\lambda,0)$ is the downwelling irradiance (W m^{-2} nm^{-1}) above the air–water interface. For a nadir looking sensor, L_w can be estimated from L_u as in Mobley (1999):

$$L_w(\lambda, 0) = \tau L_u(\lambda, 0) \tag{10}$$

where, τ is a non-dimensional proportionality factor that relates upwelling radiance measured just below the water surface to water leaving radiance. For most remote sensing applications, τ can be reasonably approximated as 0.54 (Mobley, 1999). $L_u(\lambda, 0)$ is the subsurface upwelling radiance and for uniform angular distribution, L_u can be formulated as (Jerlov, 1968):

$$L_u(\lambda, 0) = E_u(\lambda, 0)/Q \tag{11}$$

where, $E_u(\lambda,0)$ is upwelling irradiance (Wm^{-2} sr^{-1} nm^{-1}) and Q is the angular distribution factor of spectral radiance and assumed to be 4 based on the average solar zenith angle in our study area (Morel & Gentili, 1996). Finally, combining Eqs. (6)–(11), R_{rs} can be written as follows:

$$R_{rs}(\lambda) = 0.0448 \frac{b_b(\lambda)}{(a(\lambda) + b_b(\lambda))} \tag{12}$$

To model the fluorescence component of R_{rs}, water leaving radiance due to chlorophyll fluorescence at 685 nm ($L_{w,fl}(685)$) was modeled as in Gilerson et al. (2007). $R_{rs,fl}(685)$ was estimated as:

$$R_{rs,fl}(685) = \frac{L_{wfl}(685)}{E_d(685)} \tag{13}$$

Based on the Hydrolight (Mobley & Sundman, 2001) simulation as in Gilerson et al. (2007) for a clear sky condition, E_d was considered as 1.1 Wm^{-2} nm^{-1}. Finally, $R_{rs,fl}$ was modeled at every wavelength using a Gaussian peak centered at 685 nm with a standard deviation (STD) of 10.6 nm (Mobley, 1994). The final $R_{rs}(\lambda)$ values were modeled as a sum of R_{rs} estimations from Eqs. (12) and (13).

2.2. Simulation of R_{rs} data

Using the above bio-optical model, we simulated two R_{rs} datasets representing four case 2 water bodies such as Mississippi Delta region, Mobile Bay, Chesapeake Bay, and Delaware Bay. Further, assuming that there are three optically active constituents in the water (i.e. phytoplankton, suspended matter, and CDOM), the total absorption, $a(\lambda)$ coefficients can be written as follows:

$$a(\lambda) = \sum_{i=1}^{n} a_i(\lambda), \tag{14}$$

where, a_i are the absorbing components such as water (a_w), chl-a (a_{chl}), CDOM (a_{CDOM}), and non-algal particle (a_{nap}). Similarly, total backscattering coefficient can be written as:

$$b_b(\lambda) = \sum_{i=1}^{n} b_{b,i}(\lambda) \tag{15}$$

where, $b_{b,i}$ are the back-scattering components such as water (b_{bw}) and total particulate matter (b_{bp}). Phytoplankton absorption coefficient was modeled as the product of specific absorption coefficient (a_φ^*) and the chl-a concentration (C_{chl-a}). a_φ^* values were taken from Ciotti et al. (2002) as a sum of specific absorption coefficient of micro-planktons and pico-planktons with different weighting factor, S_f, ranging from 0.1 to 0.5 that corresponds to typical turbid productive coastal waters (Ciotti et al., 2002).

$$a_\varphi^*(\lambda) = S_f \cdot a_{pico}^*(\lambda) + (1 - S_f) \cdot a_{micro}^*(\lambda) \tag{16}$$

$a_w(\lambda)$ and $b_{b,w}(\lambda)$ values were taken from Pope and Fry (1997). CDOM absorption was expressed as a function of the absorption coefficient at 440 nm, $a_{CDOM}(440)$, and a slope factor, S_{CDOM}, as follows (Bricaud et al., 1981):

$$a_{CDOM}(\lambda) = a_{CDOM}(440)e^{-S_{CDOM}(\lambda - 440)} \tag{17}$$

Similar to CDOM absorption, a_{nap} was expressed as an exponentially decaying function with respect to the wavelength as:

$$a_{nap}(\lambda) = a_{nap}(443)e^{-S_{nap}(\lambda - 443)} \tag{18}$$

where, $S_{nap} = 0.0123$ nm^{-1} was taken from Babin et al. (2003). $a_{nap}(443)$ was expressed as:

$$a_{nap}(443) = (0.031)(0.81)C_{chl-a}$$

where, 0.031 and 0.81 are the mass-specific a_{nap} coefficient and C_{nap}: C_{chl-a} ratio respectively. This relationship explains the observed co-variation between a_{nap} and C_{chl-a} (Babin et al., 2003). Particulate back-scattering coefficient was expressed as:

$$b_{bp}(\lambda) = b_{b,p}^*(550)\left(\frac{550}{\lambda}\right)^y C_p \tag{19}$$

where, $b_{b,p}^*(550)$ is the specific back-scattering coefficient of particulate matter (0.0086 m^{2}g^{-1}) (Kiefer & Reynolds, 1992), y is the spectral slope of $b_{b,p}$ (set to 0 as in Dall'Olmo & Gitelson, 2006), and C_p is the concentration of particulate matter.

We used previously published ranges of $a_{CDOM}(440)$ and concentrations of inorganic suspended sediment (ISS) resembling each study region taken from Kutser et al. (2009), Miller et al. (2002), and Tzortziou et al. (2007) (Table 1). Assuming optical similarity, published values from Mississippi Sound have been considered for the Mobile Bay. The range of chl-a concentration used for the simulation widely varied

Table 1
Ranges of a_{CDOM} (440) (m^{-1}), S_{CDOM} and ISS (mg l^{-1}) from all study regions used in the bio-optical modeling of $R_{rs}(\lambda)$.

Study regions	a_{CDOM} (440) (m^{-1})	S_{CDOM}	ISS (mg l^{-1})
Mississippi River Delta	0.05–0.07	0.016	2–5
Chesapeake Bay and Delaware Bay	2.0–5.0	0.016	5–10
Mississippi Sound/Mobile Bay	3.13–4.27	0.016	2–5

from 1 to 60 mg m^{-3}. Concentrations and values of model parameters, such as chl-*a*, ISS, a_{CDOM} (440), and S_{CDOM} were randomly varied at each iteration step to mimic the natural variability in the study regions.

R_{rs} data were simulated at 1 nm interval from 400 nm to 760 nm ($n = 200$). R_{rs} measurements were further simulated at each MERIS band centers λ_i, for bands 1 to 10, by taking the weighted average of each R_{rs} spectra using the spectral response function (SRF(λ)) of MERIS (http://earth.eo.esa.int/pub/ESA_DOC/MERIS_Wavelengths_and_Irradiances_Model2004.xls) as weights (Eq. (20)). Finally, the simulated MERIS spectra were used for further analysis.

$$R_{rs}(\lambda_i) = \frac{\sum_{\lambda} R_{rs}(\lambda) SRF(\lambda)}{\sum_{\lambda} SRF(\lambda)} \quad (20)$$

2.3. Field data

The concept of NDCI was developed using simulated data, however, field datasets acquired from the same geographic regions were used to further validate the NDCI and chl-*a* relationship. The field datasets consisted of chl-*a* concentrations from Chesapeake Bay, Delaware Bay, the river Mississippi Delta region, and the Mobile Bay (Fig. 1). However, the field data were not used in the simulation because of the absence of a wide chl-*a* range, and the unavailability of other data such as inorganic suspended solid concentration (ISS), a_{CDOM} (λ), and S_{CDOM} that are required as input to the bio-optical model. In situ chl-*a* data from Chesapeake Bay and Delaware Bay ($n = 38$; collection dates: April, 15, 16, and 18, 2008, May 14, 2008) were downloaded from SeaWiFS Bio-Optical Archive and Storage System (SeaBASS) archives. Similarly, chl-*a* data for Mississippi Delta region ($n = 10$; collection date: May 19, 2007) were acquired from the NASA bio-Optical Marine Algorithm Data (NOMAD) archive. Both SeaBASS and NOMAD archives contain high quality bio-optical global datasets which are suitable for calibrating and validating ocean color algorithms (Werdell & Baily, 2005). In situ data from Mobile Bay were collected and analyzed using high performance liquid chromatography (HPLC) (by Hugh MacIntyre, Dolphin Island Sea Lab) ($n = 8$; collection date: Nov 07, 2007). The frequency plot of chl-*a* observation in all field sites is presented in Fig. 2 and the summary of chl-*a* measurements, solar zenith and solar azimuth angles of the study sites is also summarized in Table 2.

2.4. Satellite data

Simultaneous observations of full resolution level 2 data acquired by MERIS sensor onboard ENVISAT were downloaded using European Space Agency's client EOLI (Earth Observation Link) for NDCI model calibration and validation. Beam 3.6 software (Brockmann Consult, Geesthacht, Germany) was used to process and analyze the MERIS images. Image data acquired on April 15 2008 (Universal Time Coordinates−15:43:39.476) over Chesapeake Bay had some cloud cover and was masked for land and cloud. However, cloud cover over the Mississippi River Delta region and the Mobile Bay was minimal. Corresponding MERIS images over Chesapeake and Delaware Bay was not available on August 16, 2008 and therefore, image acquired on August 15, 2008 was used. Images acquired on April 18, 2008 (UTC−15:49:21.537) and May 14, 2008 (UTC−15:32:21.458) over Chesapeake Bay were also used in this study. Similarly, images

for the Mississippi Delta and the Mobile Bay were acquired on May 19, 2007(UTC−16:20:52.509) and November 07, 2007 (UTC−16:15:06.954).

MERIS level 2 products are atmospherically corrected for normalized water leaving reflectance. Corresponding R_{rs} spectra were extracted from MERIS images for the in situ sampling locations and are presented (Fig. 3B). R_{rs} spectra showed high variability in magnitude in the visible spectral domain. Maximum values of R_{rs} were observed at the green channel (559 nm) and maximum variability was also occurred at 559 nm and 620 nm. As expected, R_{rs} in the blue spectral region showed lower reflectance because of high absorption by chlorophylls, CDOM, and non-algal particulate matters in the water. A large number of pixels showed negative R_{rs} at 412.5 and 442.5 nm possibly because of over correction for the atmospheric scattering. The spectral shape of the average R_{rs} spectrum appeared very similar to the simulated data (Fig. 3A).

2.5. Model calibration and validation

NDCI model was calibrated and validated using a simulated and a field dataset. A one-fold calibration and validation was performed using the simulated dataset, whereas, a three-fold calibration and validation was performed using the field dataset. The three-fold calibration and validation to the field data was based on three varying parameters including (a) solar zenith angle (θ_s), (b) solar azimuth angle (φ_s), and (c) geographic region. In the first two calibration and validation, the field data sorted out based on solar angle parameters (θ_s, φ_s) in order to test the robustness of the model to variations observed in satellite data because of atmospheric interferences and seasonal changes, and transferability of the model to other similar coast water bodies. In the third calibration and validation, the data were sorted out based on geographic region in order to maintain the independence aspect of the field data.

The first calibration and validation dataset was sampled after sorting based on descending θ_s and further dividing the data into two subsamples, one for calibration ($n = 29$) and the other for validation ($n = 20$). Similarly, the second calibration and validation was performed after sorting the field data based on descending φ_s and further dividing into a calibration dataset ($n = 29$) and a validation dataset ($n = 20$). Remote sensing reflectance (R_{rs}), being an apparent optical property, is prone to vary with any change in the light field geometry and atmospheric conditions even though the concentrations of all the biophysical variables (TSS, chl-*a*, CDOM) remain constant in the water column. While formulating NDCI, it was hypothesized that a normalized band difference index will be less sensitive to any uncertainties because of variations in light field geometry, atmospheric effects, and radiometric calibration differences by virtue of its spectral band selection and model architecture. In the current scenario, solar zenith (θ_s) and solar azimuth angles (φ_s) have been used as a measure to represent seasonal and spatial change in light field as these solar angles change with geographic regions, and with season in a geographic region.

Finally, the third set of calibration and validation was performed by dividing the dataset from all study regions into two subsets based on geographic regions. Calibration dataset contained all sample points from the Chesapeake Bay and Delaware Bay ($n = 35$), whereas, sample points from the Mississippi Delta and the Mobile Bay were used as the validation dataset ($n = 14$). In this way, the model calibrated for a region with a specific set of bio-optical and physical characteristics will be validated for a different region with a different set of bio-optical and physical parameters demonstrating the strength and the transferability of the algorithm to other coastal regions.

For the model calibration, best fit functions were calculated based on least-squares regression analysis. Using the calibrated equations, chl-*a* concentrations were predicted for the validation dataset. The accuracy of the model prediction was assessed by comparing the
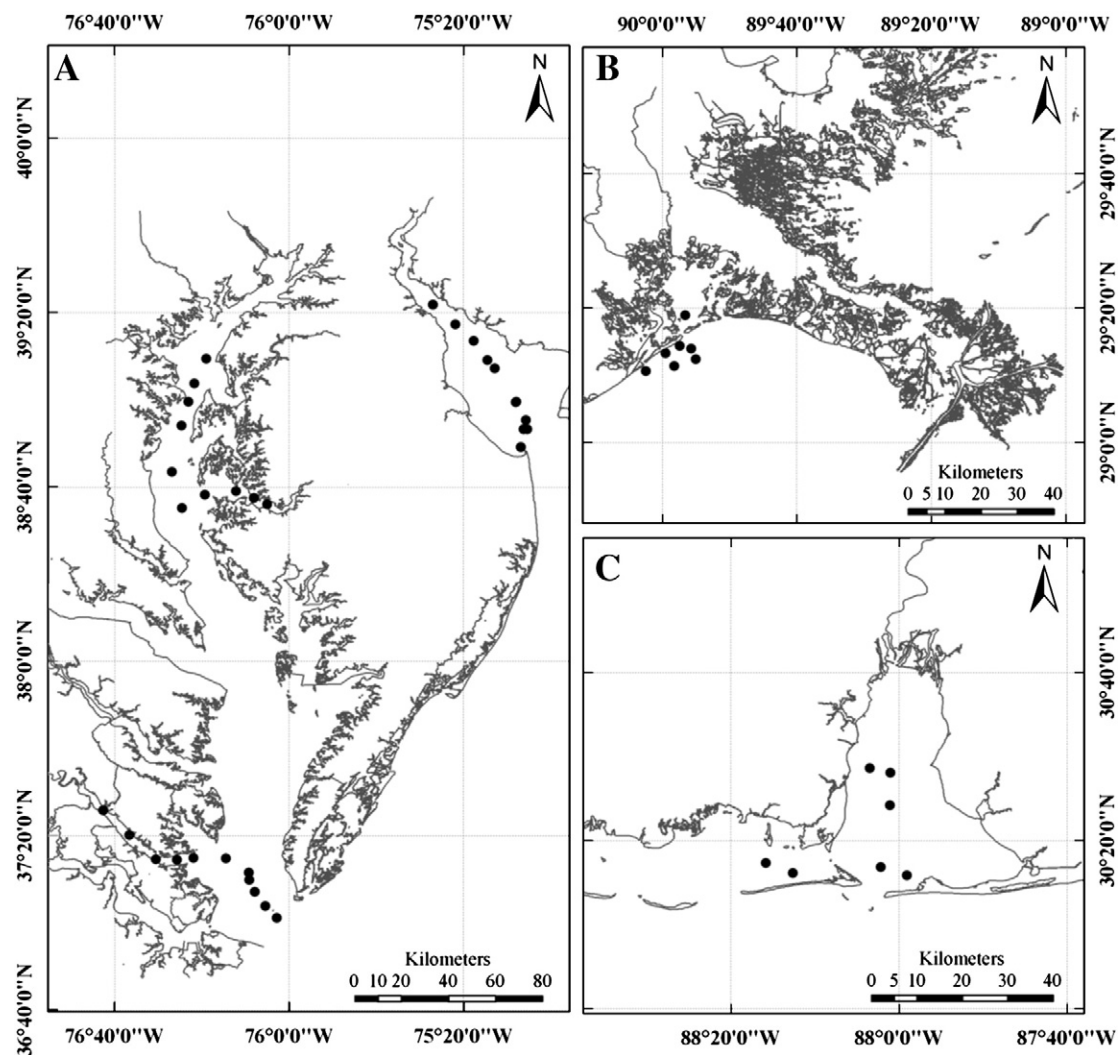
Fig. 1. Location map of data points used in the present study. (A) Chesapeake Bay and Delaware Bay, (B) River Mississippi Delta region in the northern Gulf of Mexico, and (C) Mobile Bay.

predicted chl-*a* and the measured chl-*a* concentration. The comparison was expressed in terms of root mean squared error (RMSE), coefficient of determination (R^2) between measured and predicted chl-*a*, the slope

of the best fit line (m), and the mean ratio that was calculated as the average of the ratios of the predicted chl-*a* values to the measured chl-*a* values. RMSE was computed as:

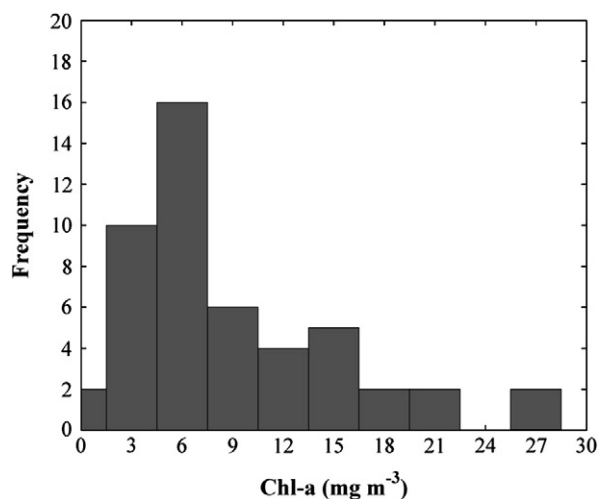$$RMSE = \sqrt{\frac{\sum_{i=1}^{n} \left(\hat{Y}_i - Y_i\right)^2}{n}} \qquad (21)$$

Fig. 2. Frequency histogram of surface chl-*a* concentration (mg m^{-3}) measured from Chesapeake and Delaware Bay, Mississippi Delta region, and Mobile Bay.

Table 2
Descriptive statistics of chl-*a* (mg m^{-3}), solar zenith and solar azimuth angles in the study regions. All angular measurements are in degree.

| Parameters	Min	Max	Average
Mississippi Delta, 19th May 2007 (n = 6)			
Chl-*a* (mg m^{-3})	14.351	28.175	21.042
Solar zenith angle	23.303	23.393	23.349
Solar azimuth angle	108.306	108.709	108.495
Chesapeake Bay and Delaware Bay (n = 35)			
Chl-*a* (mg m^{-3})	0.903	16.061	7.255
Solar zenith angle	26.958	34.196	31.492
Solar azimuth angle	131.943	144.597	140.914
Mobile Bay (n = 8)			
Chl-*a* (mg m^{-3})	4.208	6.395	5.256
Solar zenith angle	50.353	50.577	50.471
Solar azimuth angle	154.587	154.915	154.807
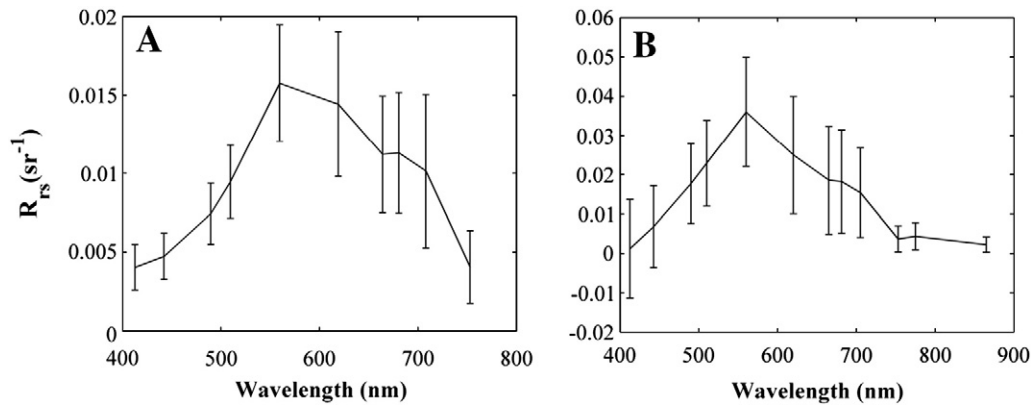
Fig. 3. Average R_{rs} spectra derived from (A) the simulated dataset ($n = 200$), (B) MERIS images of the study regions ($n = 49$). y-error bars are the one STD of R_{rs} at MERIS band centers.

where n is the number of observations, $\hat{Y}$ is the predicted value of chl-a, Y is the observed or measured value of chl-a.

3. Results

3.1. Model calibration and validation using simulated data

We compared several existing blue-green band ratio algorithms such as OC4 (O'Reilly et al., 1998, 2000) and two-band red-NIR models (T07, M09) with NDCI during model calibration. Three-band models that use R_{rs} values at 753 nm and beyond were not considered for comparison because the absorption coefficients of water and phytoplankton available in literature do not produce reliable estimates of R_{rs} beyond 750 nm (Kutser et al., 2009). Model calibration results using the blue-green band ratio showed high sensitivity to the changes in a_{CDOM} and a_{nap}. Therefore, developing a single empirical relationship using blue-green band ratios during model calibration was not possible because of the absence of a common trend line for all study areas (not shown). In contrast, red-NIR based models showed a single trend for all study areas indicating their insignificant sensitivity to the changes in a_{CDOM} and a_{nap}.

Various linear and nonlinear trend lines were fitted to the data and best outputs were finalized and reported for all models (Table 3). Relationship between NDCI and chl-a was essentially nonlinear. However, logarithmic and power trend lines could not be fitted to the data because of the negative NDCI values. An exponential function with two-parameters explained 93% of variance in the data ($R^2 = 0.93$, standard error of the estimate (STE) = 4.38 mg m^{-3} of chl-a, $p < 0.0001$) where as a second order polynomial produced the highest R^2 and lowest estimation error ($R^2 = 0.95$, STE = 3.62 mg m^{-3} of chl-a, $p < 0.0001$) in the simulated dataset (Table 3). Quadratic polynomial equation was finally selected as the final NDCI-chl-a equation because of higher R^2 and lower STE. Unlike NDCI, linear relationships were found between the two-band models and chl-a during model calibration. STE and R^2 for M09 were 3.76 mg m^{-3} and 0.95 ($p < 0.0001$) respectively. T07 showed a weak relationship with chl-a in the model calibration stage with STE and R^2 of 10.76 mg m^{-3} and 0.61 ($p < 0.0001$) respectively.

Table 3
Model calibration: all model parameters including a_0, a_1, and a_2 with corresponding standard error of estimate (STE) are provided; In case of linear regression, a_0 and a_1 correspond to intercept and slope of the fitted equation. Coefficient of determination (R^2), adjusted R^2 and p values of the regression models are also provided.

Indices	a_0	a_1	a_2	R^2	Adj. R^2	STE of estimate	p
Simulated dataset ($n = 100$)							
NDCI	42.197	236.5	314.97	**0.95**	**0.95**	**3.62**	<0.0001
M09	−64.055	106.335	*	0.95	0.95	3.76	<0.0001
T07	−39.739	102.717	*	0.61	0.61	10.76	<0.0001
Field dataset (solar zenith angle, $n = 29$)							
NDCI	14.039	86.115	194.325	**0.90**	**0.89**	**2.49**	<0.0001
M09	−15.617	31.133	*	0.82	0.81	3.24	<0.0001
D05	14.07	177.56	808.03	0.56	0.52	5.22	<0.0001
T07	−1.832	26.56	*	0.48	0.47	5.53	<0.0001
Field dataset (solar azimuth angle, $n = 29$)							
NDCI	14.279	79.607	181.45	**0.90**	**0.90**	**2.11**	<0.0001
M09	−15.992	31.196	*	0.85	0.84	2.61	<0.0001
D05	14.15	156.88	769.86	0.49	0.45	4.93	0.001
T07	4.643	15.473	*	0.20	0.17	6.08	0.0134
Field dataset (Chesapeake Bay and Delaware Bay, $n = 35$)							
NDCI	13.55	87.99	212.6	**0.72**	**0.7**	**2.15**	<0.0001
M09	−8.88	20.96	*	0.59	0.58	2.57	<0.0001
D05	11.52	136.13	666.46	0.43	0.4	3.09	<0.0001
T07	6.0	3.164	*	0.01	0.0	4.02	0.4394

Data in bold letter highlights the best performing model with the highest R^2 and lowest STE during the calibration stage.
* Not applicable.

Table. 4
Model validation results: root-mean-square-error (RMSE) in mg m^{-3}, coefficient of determination (R^2), and the slope of the regression line (m) are reported for all models. The RMSE, R^2, and m values of the predictions are provided (a) for data points within the calibrated chl-a range (values outside the brackets) and (b) for the entire dataset (values inside the bracket).

Indices	RMSE (mg m^{-3})	R^2	m
Simulated dataset ($n = 100$)			
NDCI	**4.83**	**0.93**	**1.05**
M09	5.26	0.92	1.07
T07	21.78	0.26	0.57
Field dataset (solar zenith angle, $n = 20$)			
NDCI	**1.89**	**0.80**	**1.005**
M09	3.27	0.80	1.115
D05	1.97	0.81	0.795
T07	10.013	0.54	−0.544
G08	4.066	0.83	0.574
MERIS	5.856	0.74	0.403
Field dataset (solar azimuth angle, $n = 16$)			
NDCI	2.04	0.34	**0.64**
M09	3.08	0.31	0.22
D05	2.46	0.06	0.34
T07	8.01	0.07	0.09
G08	3.56	0.48	0.22
MERIS	**1.69**	0.33	0.44
Field dataset (Mobile Bay and Mississippi Delta, $n = 14$)			
NDCI	**1.43 (2.37)**	**0.94 (0.92)**	**0.88 (0.91)**
M09	2.82 (5.17)	0.92 (0.94)	0.49 (0.45)
D05	2.69 (6.49)	0.91 (0.62)	0.51 (0.45)
T07	5.49 (10.08)	0.53 (0.04)	−0.06 (−0.01)
G08	4.95	0.92	1.43
MERIS	7.3	0.94	2.29

Data in bold letter highlights the best performing model with the lowest RMSE, highest R^2 and m close to 1 during the validation stage.
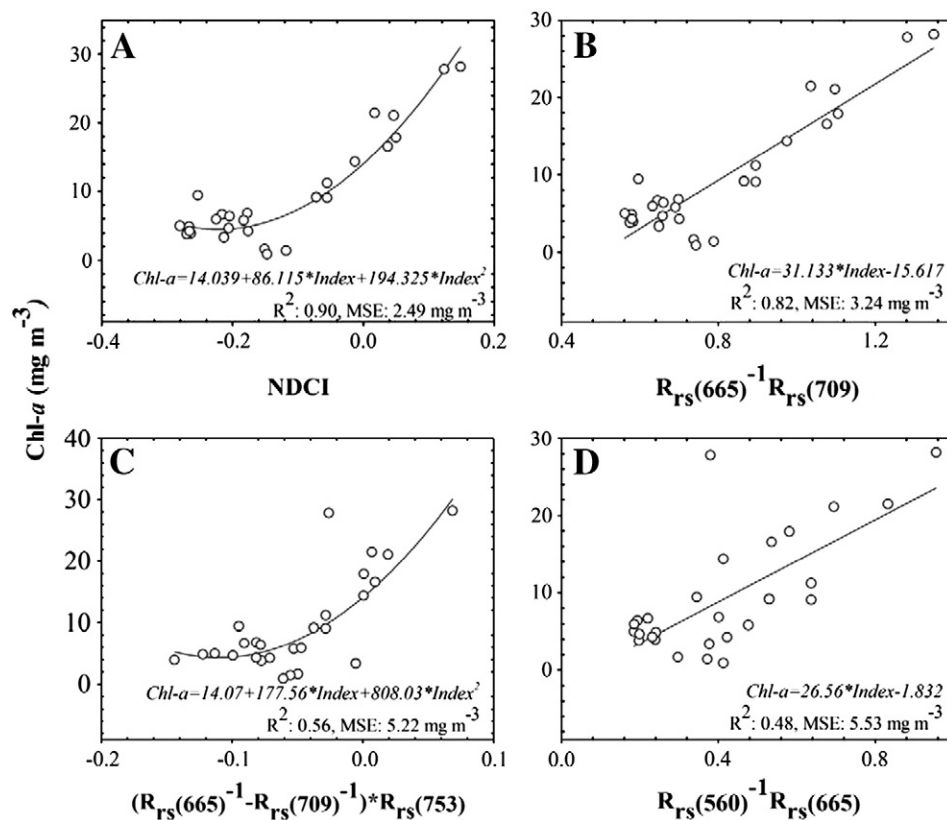
Fig. 4. Calibration plots from the first calibration dataset that was sampled based on solar zenith angle: (A) NDCI, (B) M09, (C) D05, and (D) T07.
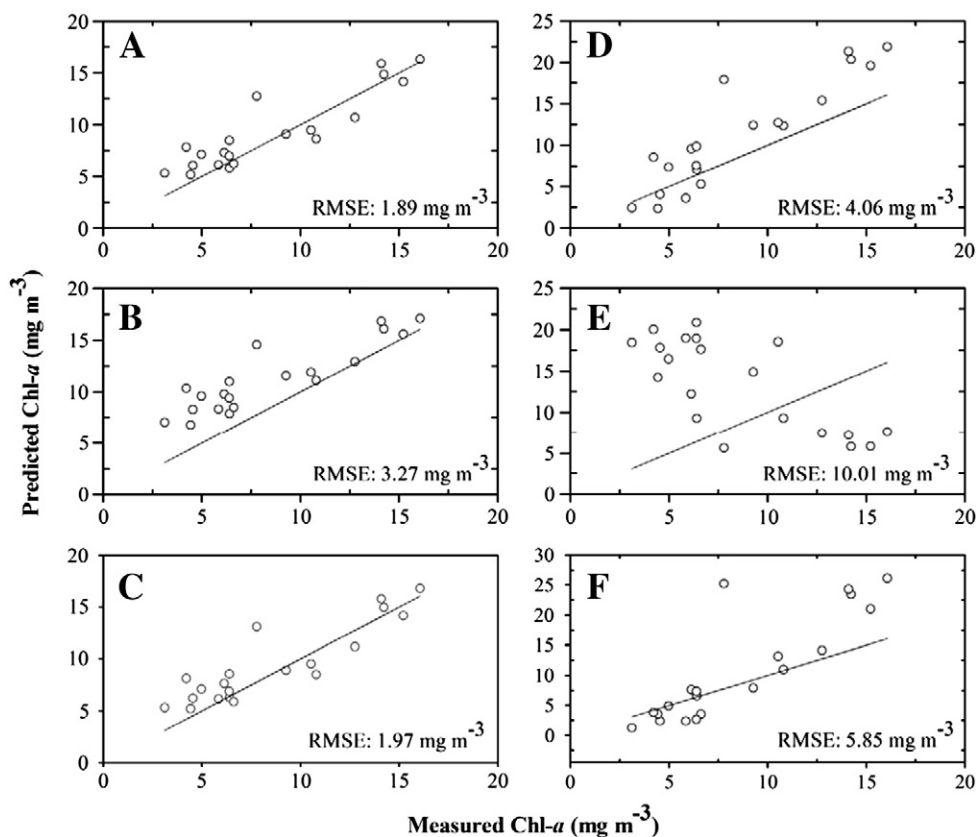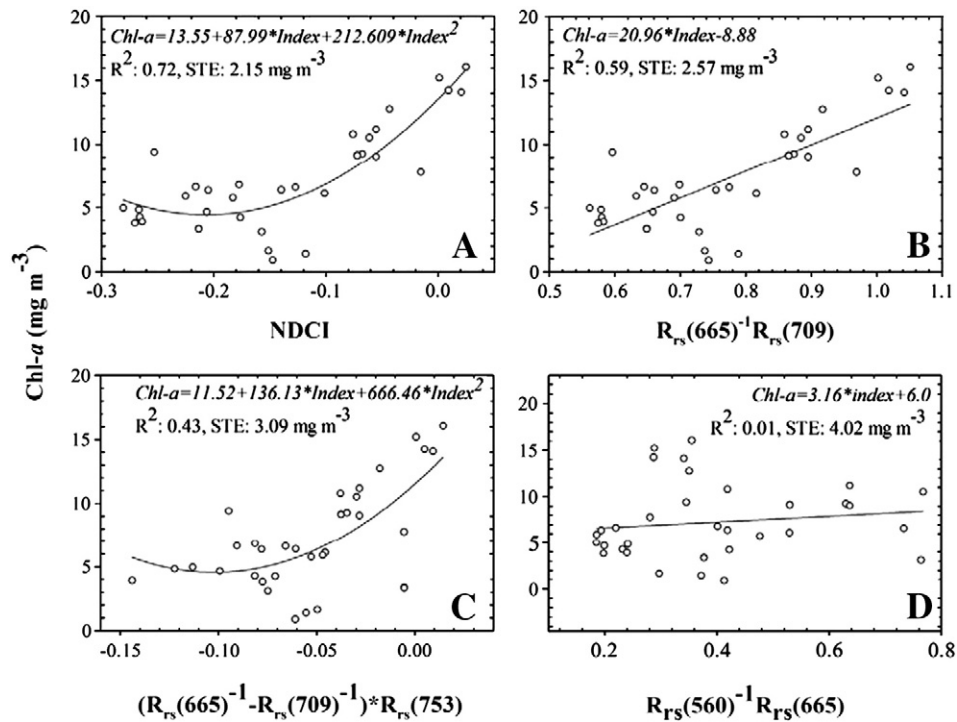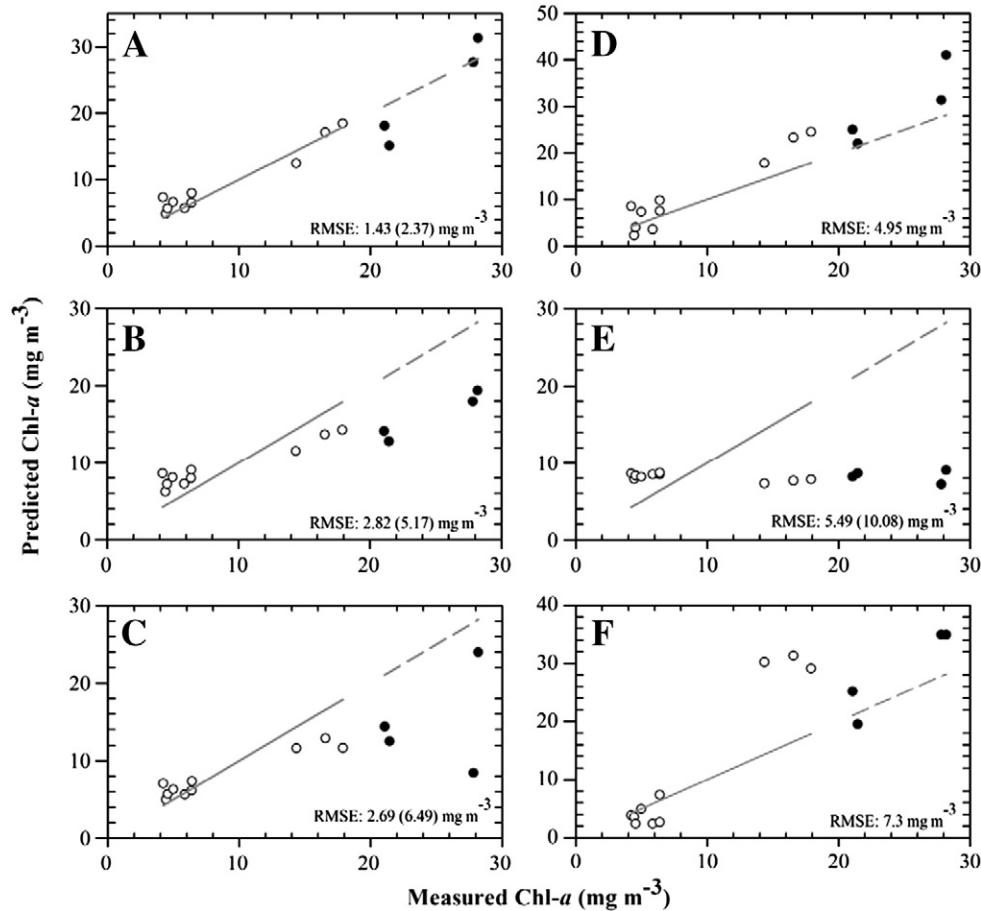

Fig.5. Validation plots from the first validation dataset that was sampled based on solar zenith angle: (A) NDCI (B) M09, (C) D05, (D) G08, (E) T07, and (F) MERIS case 2 chl-*a* product (Algal-2). Straight lines on the plots are the 1-to-1 lines.

Fig. 6. Calibration plots from the third calibration dataset that was sampled based on geographic region: (A) NDCI, (B) M09, (C) D05, and (D) T07. The calibration dataset contained data points from the Chesapeake Bay and Delaware Bay.

Fig. 7. Validation plots from the third validation dataset that was sampled based on geographic region: (A) NDCI (B) M09, (C) D05, (D) G08, (E) T07, and (F) MERIS case 2 chl-*a* product (Algal-2). Validation dataset contained data points from the Mobile Bay and the River Mississippi Delta. Solid circles represent the predictions outside of the calibrated chl-*a* range. Solid and dashed lines are the 1:1 lines for the predictions inside and outside of the calibrated chl-*a* range respectively. RMSE of the predictions within the calibrated chl-*a* range (values outside the brackets) and the RSME of the entire dataset (values inside the bracket) are provided.

All calibrated models were examined for their predictive ability and transferability to other geographic regions (Table 4). Using the calibration equation, chl-a values were predicted for an independently modeled dataset and were compared with actual chl-a concentrations. NDCI produced a root mean squared error (RMSE) of 4.83 mg m^{-3}, whereas, M09 and T07 produced RMSE of 5.26 and 21.78 mg m^{-3} respectively. NDCI produced the most accurate prediction showing highest coefficient of determination ($R^2 = 0.93$) between actual and predicted chl-a and the slope of the regression line was close to 1 ($m = 1.05$). On the simulated dataset, M09 performance was similar to NDCI with $R^2 = 0.92$ and $m = 1.07$ and T07 model predicted significantly inaccurate values. The residuals from NDCI and M09 validation did not reveal a trend of over or under estimation; however, residuals from T07 had a clear trend of over estimation (not shown).

3.2. Model calibration and validation using field data

Two sets of calibration/validation were performed on selected models based on the solar zenith and solar azimuth angles on MERIS data from all study regions (Table 3). Similar to the simulated data calibration results, in the field data calibration based on solar zenith angle, NDCI showed a strong relationship with chl-a concentration (quadratic function) producing R^2 and STE of 0.90 and 2.49 mg m^{-3} respectively ($p < 0.0001$) (Fig.4). A two parameter-exponential trend line was also fitted that explained 87% of variance in the data ($R^2 = 0.87$, STE = 2.7 mg m^{-3} of chl-a, $p < 0.0001$). However, quadratic polynomial equation was finally selected because of higher R^2 and lower STE. M09 performed as the second best model with R^2 of 0.82 and STE of 3.24 mg m^{-3} ($p < 0.0001$), however, the performance gap between NDCI and M09 was found to be higher in field data compared to the simulated data. Unlike the expected linear relationship between D05 and chl-a (Dall'Olmo & Gitelson, 2005), a quadratic function explained the maximum variance in the data ($R^2 = 0.56$, $p < 0.0001$) producing a STE of 5.22 mg m^{-3}. T07 model produced the least R^2 (0.48) and highest STE value (5.53 mg m^{-3}, $p < 0.0001$).

All four models plus G08 and MERIS level-2 chl-a product (Algal-2) were validated using the corresponding validation dataset (Fig. 5; Table 4). G08 was not parameterized and the chlorophyll equation from Gons et al. (2008) was used for validation. NDCI performed the best with the least RMSE (1.87 mg m^{-3}), high R^2, $m \approx 1$, and no clear residual trend of over or under-estimation. T07 produced the highest RMSE (10.01 mg m^{-3}) and the least R^2. Performance of the 3-band model, D05, was close to NDCI in the validation stage producing RMSE of 1.97 mg m^{-3} and M09 showed a clear trend of over estimation (Fig. 5). G08 had a RMSE of 4.06 mg m^{-3} and showed a trend of over-estimation for all predictions greater than 7 mg m^{-3}. MERIS product (Algal-2) showed excellent prediction for chl-a concentration below 13 mg m^{-3} with a few exceptions (Fig. 5).

Very similar trend in results were observed with the second calibration dataset based on solar azimuth angle (Table 3). NDCI showed the strongest relationship with chl-a ($R^2 = 0.90$, STE = 2.11 mg m^{-3}, $p < 0.0001$), whereas, M09 explained 82% variation in the data and produced a STE of 2.61 mg m^{-3} ($p < 0.0001$). Neither a linear nor a quadratic function explained the relationship between D05 and chl-a very well, therefore the R^2 was low and the STE was high. Similarly, T07 model showed weakest relationship with chl-a producing lowest R^2 and highest STE values ($p = 0.0134$). Validation results showed that the MERIS Algal-2 chl-a product produced the least RMSE (1.69 mg m^{-3}), however, the R^2 between predicted and actual was low and the regression slope was significantly lower than 1 (Table 4). In contrast, NDCI produced a RMSE of 2.04 mg m^{-3} with the regression slope near 1. D05 and G08 produced a RMSE of 2.46 and 3.56 mg m^{-3} respectively. Also, G08 produced high estimation errors for low chl-a values (oligotrophic waters) with five negative prediction. Similar to the previous validation, T07 model produced the highest RMSE and proved to have the least predictive ability.

Finally, the last set of calibration and validation was performed on the datasets those were sampled based on geographic regions. Similar to the previous calibration results, NDCI showed the strongest relationship with measured chl-a ($R^2 = 0.72$, STE = 2.15, $p < 0.0001$) and the weakest relationship was found between T07 and chl-a ($R^2 = 0.01$, $p = 0.439$) (Table 3, Fig. 6). Note that the third validation dataset contained four points with chl-a concentration higher than the chl-a concentration range used in the calibration. Therefore, the validation results for all models are shown in two ways including (a) data points within the calibration range (values outside the brackets) and (b) the entire dataset (values inside the bracket) (Table 4, Fig. 7). Validation results show that NDCI was successful predicting chl-a concentration with highest accuracy producing a RMSE of 1.43 (2.37) mg m^{-3}. The R^2 between the measured and predicted chl-a was 0.94 with a regression slope of 0.88 (0.91). Algal-2 showed maximum prediction error with two-fold over estimation. It is also evident that, unlike other calibrated models, predictions by the NDCI equation outside its calibration range was also very accurate and the equation can be reliably used to predict chl-a up to 28.17 mg m^{-3} (Fig. 7).

It should be noted that in the simulated and the first field dataset, NDCI showed the most accurate predictive ability overall with no trend in residuals (Fig. 8). However, in the second validation dataset three different models performed best in three different categories. G08 produced the highest R^2, Algal-2 produced the least RMSE, and NDCI produced a regression slope closest to 1. Similarly, NDCI showed excellent prediction in the third validation dataset producing lowest RMSE, highest R^2 between predicted and actual chl-a and m close to 1.
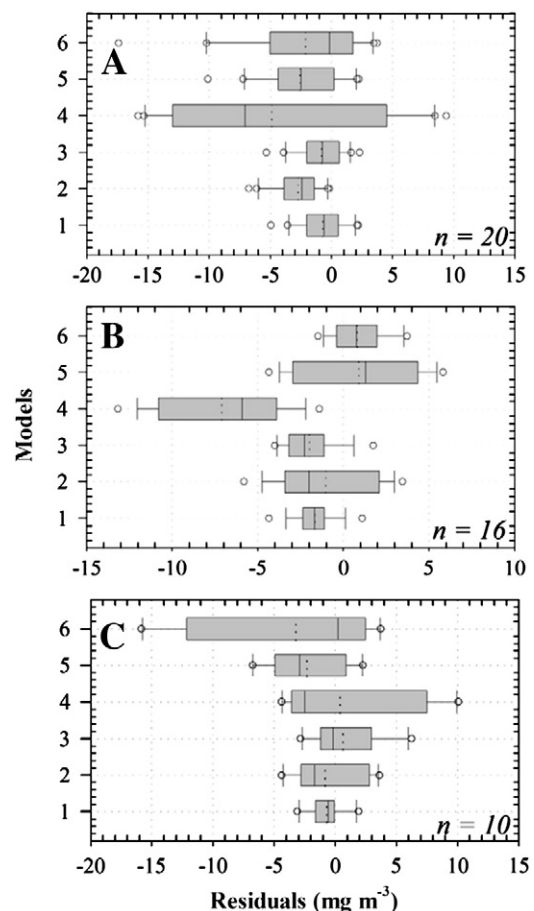

Fig. 8. Box plots showing residuals from three fold validation, (A) dataset based on solar zenith angle, (B) dataset based on solar azimuth angle, and (C) dataset based on geographic regions of all models such as (1) NDCI, (2) M09, (3) D05, (4) T07, (5) G08, and (6). MERIS chl-a product (Algal-2). The dotted lines inside boxes are the mean lines.

Table 5
Comparison of mean ratio (STANDARD DEVIATION) of modeled and measured chl-*a* for all field regions combined, Chesapeake Bay, Mobile Bay, and Mississippi Delta region.

Models	All Regions	Chesapeake and Delaware Bay	Mobile Bay	Mississippi Delta
NDCI	**1.12 (0.29)**	**1.07 (0.28)**	1.32 **(0.28)**	**0.95 (0.12)**
M09	1.47 (0.42)	1.31 (0.38)	1.76 (0.36)	0.93 (0.11)
D05	1.17 (0.31)	1.09 (0.29)	1.33 (0.30)	0.81 (0.22)
T07	2.20 (1.60)	1.48 (1.52)	3.52 (0.62)	0.70 (0.15)
G08	1.26 (0.43)	1.30 (0.38)	**1.17 (0.54)**	1.26 (0.16)
MERIS	1.11 (0.65)	1.31 (0.70)	0.74 (0.30)	1.46 (0.43)

Mean ratio = average of the ratios of the predicted chl-*a* values to the measured chl-*a* values.

However, if all the three validation parameters are considered simultaneously, NDCI showed overall better predictive ability (Table 4, Fig. 8). Thus, the three-fold calibration resulted in three sets of chl-*a* equations with coefficients very close to each other. The difference among them causes minimal impact on the prediction accuracy of the models. It has been verified by applying all three NDCI equations on an independent validation dataset (validation dataset 3) and the very similar results were observed. All three equations produced a RMSE very close to 2.37 mg m^{-3} with a STD of 0.127 mg m^{-3} mg m^{-3} of chl-*a* (not shown).

3.3. Chlorophyll mapping using MERIS data

MERIS images acquired on April 15, 2008 were selected for the Chesapeake and Delaware Bay for mapping spatial distribution of chl-*a*. Image preprocessing steps included georeferencing and land and cloud masking. We also masked out pixels with inaccurate reflectance values (mostly negative values) and Open Ocean or case 1

areas. NDCI chl-*a* equation generated from the first calibration dataset (based on solar zenith) was applied on MERIS images from Chesapeake and Delaware Bay, Mississippi Delta region, and the Mobile Bay to prepare chl-*a* distribution maps. As shown in validation results, NDCI was successful in predicting chl-*a* concentration with a 12% overall bias for all regions (Table 5). chl-*a* estimation accuracy for Chesapeake Bay and the Mississippi Delta were within 5–7% of the measured in situ values, whereas, the bias in Mobile Bay was 32% (Table 5). Overall, MERIS derived chl-*a* distribution maps were consistent with the published chl-*a* levels for the Chesapeake Bay and the Mississippi Delta. The maximum chl-*a* concentration value mapped on the images was 59.08 mg m^{-3} (Figs. 9 and 10). For further analysis, all case 2 water pixels were sampled and chl-*a* values were analyzed. Frequency plot of the mapped chl-*a* in Chesapeake and Delaware Bay shows that the chl-*a* concentration in the majority of the bay was within 7–25 mg m^{-3} on July 15, 2008 (Figs. 9, 10C). In the upper Chesapeake Bay and along the shorelines, chl-*a* concentration was comparatively higher. All tributary rivers in the middle Bay region also showed higher chl-*a* concentration (Fig. 9A).

Significant portion of the MERIS image acquired on May 19, 2007 covering Mississippi Delta was of poor quality. Most of the pixels were flagged by MERIS atmospheric correction scheme with inaccurate reflectance measurements and therefore masked out. The maximum chl-*a* concentration observed in the map was 58.9 mg m^{-3} (Fig. 9B) and the frequency plot revealed that most of the pixels had chl-*a* values within 10–30 mg m^{-3} (Fig. 10B). High concentration of chl-*a* was observed in the eastern boundary of the delta.

The highest level and the range of frequently occurring chl-*a* concentration recorded on the Mobile Bay map derived from the cloud free MERIS image were 58.46 mg m^{-3} and within 7–20 mg m^{-3} respectively (Fig. 10C). As expected, north-shore of the bay showed the highest chl-*a* concentration. Because the Mobile River and the
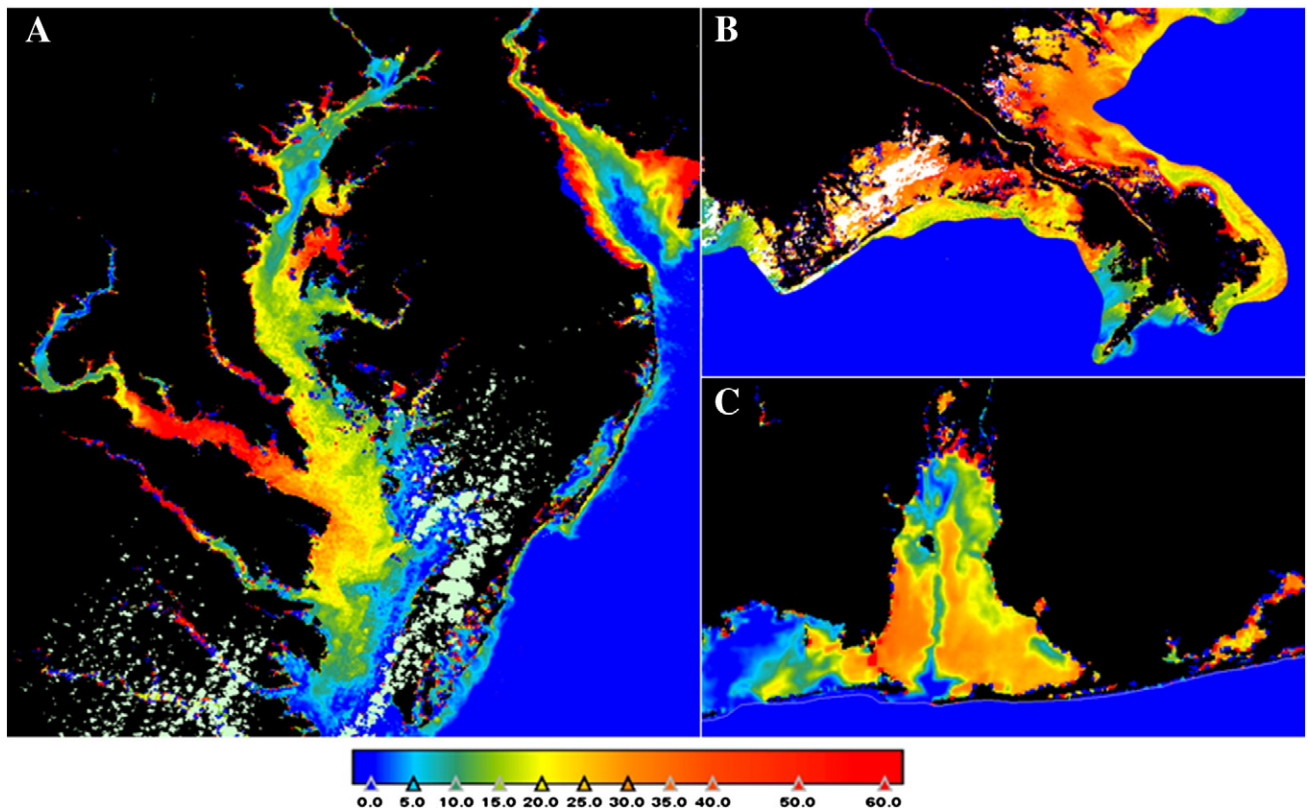
Fig. 9. (A) Spatial distribution of chl-*a* map in Chesapeake Bay, upper Bay: north of 39°N, mid-Bay (37.5°N–39°N), and lower-Bay (south of 37.5°N). Delaware Bay is located in the north–east corner, (B) Spatial distribution of chl-*a* in Mississippi delta region (pixels with no data were shown in white), and (C) in the Mobile Bay. Light green patches in the figure are clouds and the black and blue color represents land and open oceans respectively. Concentration of chl-*a* are in mg m^{-3}.
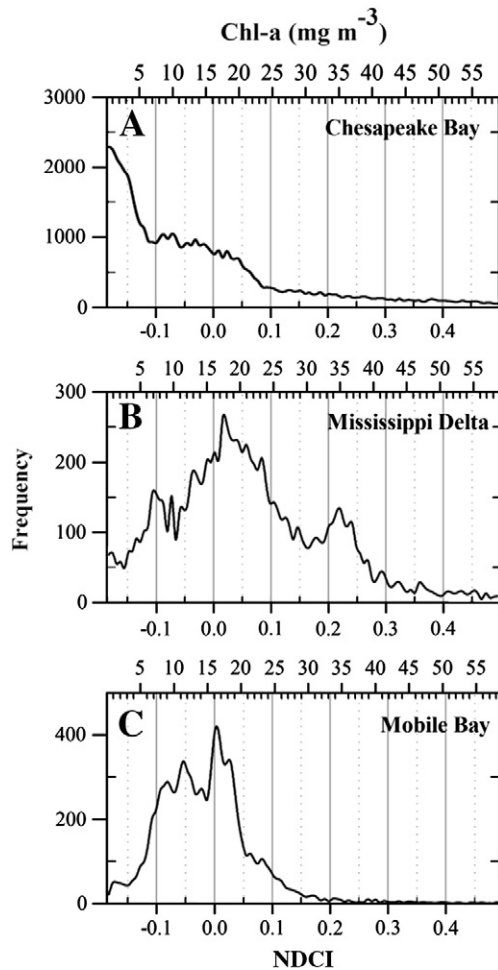
Fig. 10. Relationship between NDCI range and chl-*a* concentration at three unique case 2 water bodies. (A) Chesapeake Bay, (B) Mississippi Delta, and (C) Mobile Bay.

Tensaw River drains nutrient-rich water which stimulates the growth of phytoplankton and primary production making it the most productive part of the estuary.

4. Discussion

4.1. Algorithm performance

Accurate quantification and mapping of chl-*a* concentration in turbid productive waters using remote sensing data can create enormous opportunities for biogeochemists and climate scientists to understand the functioning of global nutrient cycles. As discussed earlier, chl-*a* mapping in turbid productive waters is often challenging because of the effect of other optically active constituents such as CDOM, detritus, and mineral particles whose concentration do not co-vary with chl-*a* (Morel & Prieur, 1977). Performances of NDCI and M09 model on the simulated calibration dataset were very similar although the standard error of the estimation for NDCI was less than the M09 model. However, NDCI produced higher R^2 and less STE than the M09 in the field dataset. Both algorithms outperformed T07 at the calibration stage. The simulated dataset was produced by varying all possible bio-optical parameters mimicking the natural variations in the Chesapeake Bay, Mississippi Delta, and the Mobile Bay. The basic difference between the two datasets was the possible existence of the remnant atmospheric contamination in the field dataset. This implies that M09 is probably more sensitive to the atmospheric parameters than NDCI and thus produced lower R^2 and higher STE with the field dataset. Since T07 uses a green channel at 560 nm, it is highly sensitive to CDOM and detritus in the water and thus produced the highest STE and RMSE in all stages of calibration and validation (Tables 3 and 4).

Consistent performance of NDCI among all models in all study regions was evident from the lowest STD of the mean ratio of 0.29 (Table 5). In contrast, MERIS Level2 chlorophyll product (Algal-2) performed poorly in all study regions with highest STD of 0.65. NDCI also produced the least bias, e.g., 7% and 15% in the Cheasepeake-Delaware Bay and in the Mississippi Delta respectively. Similarly, NDCI produced a mean ratio of 1.32 with the lowest STD of 0.28 in the Mobile Bay (Table 5).

4.2. Chlorophyll mapping using MERIS data

R_{rs} spectra sampled from the MERIS images were very similar in shape but higher in magnitude when compared to some of the published spectra from the same regions (Dall'Olmo & Gitelson, 2005; Darecki et al., 2003; Moses et al., 2009). This is because of the differences in the interpretation of R_{rs}. For example, Simis (2006) considered normalized water leaving reflectance, the radiometric quantity available from MERIS Level 2 products, $[\rho_w]_N$, as an equivalent of R_{rs}. However, if we notice the formulation of both radiometric measurements, $[\rho_w]_N$ is a product of R_{rs} and a constant, π, which could be the reason of higher magnitude of sampled spectra from MERIS images. Most of the spectra from the Chesapeake Bay exhibited an absorption feature centered at 620 nm (MERIS channel 6) which implies the presence of phycocyanin in the bay waters. Phycocyanin is widely accepted as a characteristic photopigment in cyanobacteria. Thus, the above mentioned distinct optical signature implies abundance of cyanobacteria in the Chesapeake Bay during summer months. Spectra from the river Mississippi Delta region and the Mobile Bay lacked this optical feature. In all study regions, some pixels produced extremely inaccurate estimation of chl-*a* (extreme negative and positive
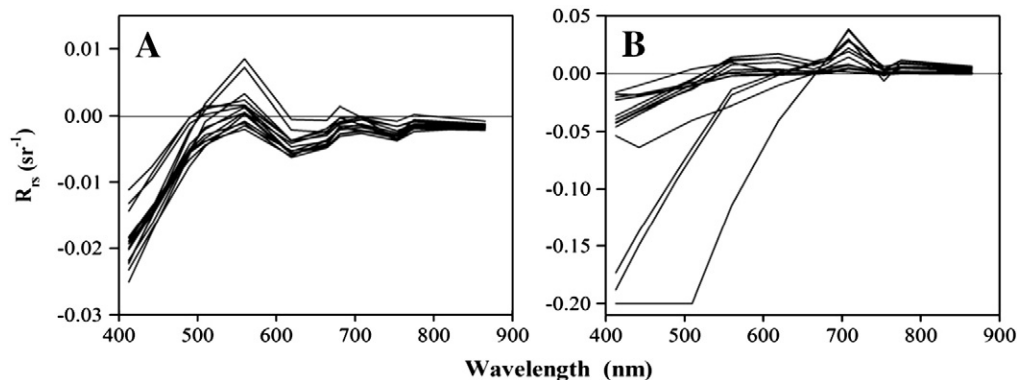

Fig. 11. Typical reflectance spectra of contaminated pixels in MERIS Level 2 reflectance product. (A) Spectra that produced extreme negative chl-*a* concentration, and (B) Spectra that produced extreme positive predictions.

Table 6
Qualitative comparison between NDCI and chl-*a* concentration from all study regions.

NDCI range	Chl-*a* range (mg m^{-3})
<−0.1	<7.5
−0.1 to 0	7.5–16
0 to 0.1	16–25
0.1 to 0.2	25–33
0.2 to 0.4	33–50
0.4 to −0.5	>50
0.5 to 1	Severe bloom

values). Reflectance spectra were randomly extracted from those extreme pixels and analyzed. All spectra showed unusual spectral shape and negative reflectance values at several spectral channels (Fig. 11). Those contaminated pixel values are believed to be originated from inaccurate atmospheric correction scheme. Those contaminated pixels were masked out from the final chlorophyll map products.

4.2.1. Chl-a and NDCI relationship

One of the biggest advantages of NDCI is that its range varies between −1 and +1 for areas with no cloud cover and adjacency and bottom effects. Therefore, qualitative chl-*a* mapping (such as NDVI for vegetation) and bloom detection using satellite data is possible for remote areas where field data is unavailable or unusable. Further analysis of the relationship between NDCI and chl-*a* helped us to associate an approximate chl-*a* range with certain NDCI values which has tremendous application and will make mapping of chl-*a* more accurate for remote areas. Based on the absorption properties and the spectral band structure of NDCI, in optically clear water bodies NDCI is expected to hold values closer to −1. NDCI values in water bodies

with moderate to high algal biomass are expected to vary in the range of −0.3 to close to 1. In case of algal blooms with surface scum on water bodies, NDCI values would vary within a range of 0.5 to 1 (Table 6). To reinforce the validity of the NDCI and chl-*a* range relationship, MERIS images of two entirely different areas,1) a mesotrophic water body (Lake Pontchartrain, LA, USA), and 2) an eutrophic inland water body (Lake Apopka, FL, USA) were considered. Lake Pontchartrain is a large, shallow, oligohaline, and semienclosed estuary located in southeastern Louisiana, USA. MERIS image acquired on October 14, 2010 is shown in true color composite and corresponding NDCI map is also shown (Fig. 12A and B). NDCI values ranged between 0.4 to around 0 qualitatively suggesting chl-*a* concentration below ~20 mg m^{-3} which is evident from the true color composite (Fig. 12A and B). On the other hand, lake Apopka is a large (surface area = 124 km^2), shallow (mean depth = 1.7 m), hyper eutrophic inland lake located in central Florida, USA and notorious for high nutrient concentrations and phytoplankton biomass (Carrick & Schelske, 1997). During summer months (April–July), chlorophyll concentration in the lake Apopka reaches as high as 105 mg m^{-3} (Carrick & Schelske, 1997). MERIS image of the lake acquired on April 29, 2010 is shown in true color and along with the corresponding NDCI map (Fig. 12C and D). The true color composite shows a severe phytoplankton algal bloom in the lake that gives the lake water a deep green hue such as terrestrial vegetation. Most frequently occurring NDCI values in the lake varies from 0.4 to 0.6 implying a severe bloom condition in the lake corresponding very well with data from literatures. Similarly, severe algal bloom was evident in the Lake Harris and the Lake Eustis in the same MERIS image (Fig. 12C).

4.2.2. Possible sources of estimation error

Errors associated with atmospheric correction of the MERIS imageries produced extreme negative and positive estimations of chl-*a* over a few
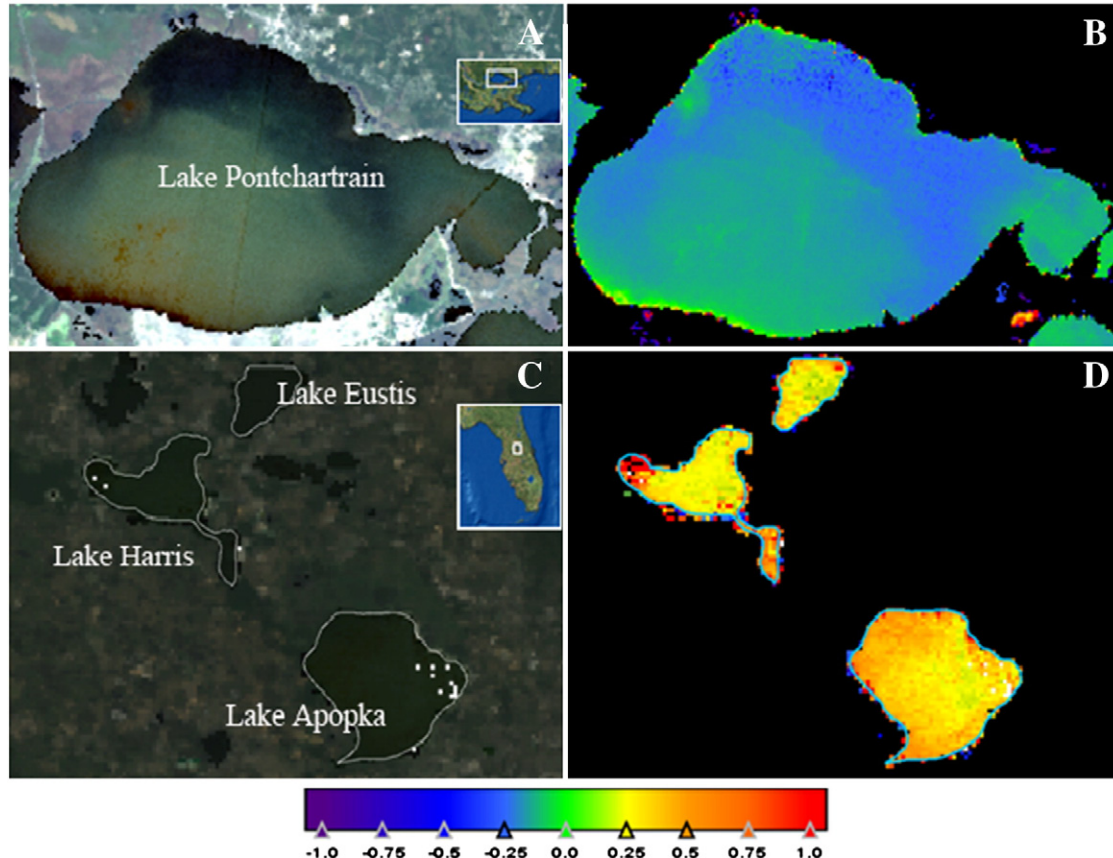
Fig. 12. (A) True color MERIS image of Lake Pontchartrain, LA, USA acquired on October 14, 2010, (B) Corresponding NDCI image, (C) True color MERIS image of Lake Apopka, Lake Harris, and Lake Eustis, FL, USA, acquired in April 29, 2010 (White color represents pixels with no data), and (D) Corresponding NDCI image. Location maps are provided in insets.

pixels in all study regions. In ocean color remote sensing studies, accuracy of the atmospheric correction scheme controls the accuracy of the mapped biophysical variable because the errors from the atmospheric correction stage are propagated to the final product. Based on the spectral band architecture of NDCI, it is clear that it would predict higher chl-*a* values upon increase in the difference between $R_{rs}(708)$ and $R_{rs}(665)$. Any disproportionate increase or decrease in reflectance at 665 and 708 nm creates inaccurate estimations of chl-*a*. For example, pixels with disproportionate increase in reflectance at 665 nm as compared to 708 nm will produce extreme negative values ; similarly disproportionate increase in reflectance at 708 nm will estimate extreme positive values of chl-*a*.

Seven in situ data points sampled from the Chesapeake and Delaware Bay on July 16 2008 did not have corresponding MERIS image and used MERIS reflectance product from July 15, 2008. Next day image was used based on the assumption that the overall concentration and spatial distribution of biomass does not change within a day. Similar assumption has also been made while using MERIS data previously (Gons et al., 2008; Moses et al., 2009). In reality, this assumption might not hold true as the water circulation in estuarine and coastal environment is very dynamic in nature. This might have caused some uncertainties in model calibration and validation.

5. Conclusion

We have presented a new index, NDCI, to be used on remotely sensed data to predict chl-*a* concentrations in optically complex turbid productive waters. We have tested its accuracy and potential applicability by extensively calibrating and validating it on (1) simulated, and (2) MERIS data representing three unique study areas with a wide range of trophic status and optical complexity. The results presented in this paper illustrate the potential of NDCI to quantify chl-*a* concentration when used with remote sensing reflectance data from MERIS sensor. We have also analyzed and presented the quantitative interpretation of NDCI values in the absence of field data and for remote areas, which makes NDCI widely applicable to coastal waters as NDVI to terrestrial vegetation.

Acknowledgment

References

Babin, M., Stramski, D., Ferrari, G. M., Claustre, H., Bricaud, A., Obolensky, G., et al. (2003). Variations in the light absorption coefficients of phytoplankton, nonalgal particles, and dissolved organic matter in coastal waters around Europe. *Journal of Geophysical Research-Oceans*, 108(C7), 3211.

Bricaud, A., Morel, A., & Prieur, L. (1981). Absorption by dissolved organic matter of the sea (yellow substance) in the UV and visible domains. *Limnology and Oceanography*, 26, 43–53.

Carder, K. L., & Steward, R. G. (1985). A remote-sensing reflectance model of a red-tide dinoflagellate off west Florida. *Limnology and Oceanography*, 30, 286–298.

Carrick, H. J., & Schelske, C. L. (1997). Have we overlooked the importance of small phytoplankton in productive waters? *Limnology and Oceanography*, 42, 1613–1621.

Ciotti, A. M., Lewis, M. R., & Cullen, J. J. (2002). Assessment of the relationships between dominant cell size in natural phytoplankton communities and the spectral shape of the absorption coefficient. *Limnology and Oceanography*, 47, 404–417.

Dall'Olmo, G., & Gitelson, A. (2005). Effect of bio-optical parameter variability on the remote estimation of chlorophyll-*a* concentration in turbid productive waters: Experimental results. *Applied Optics*, 44, 412–422.

Dall'Olmo, G., & Gitelson, A. A. (2006). Effect of bio-optical parameter variability and uncertainties in reflectance measurements on the remote estimation of chlorophyll-*a* concentration in turbid productive waters: Modeling results. *Applied Optics*, 45, 3577–3592.

Darecki, M., Weeks, A., Sagan, S., Kowalczuk, P., & Kaczmarek, S. (2003). Optical characteristics of two contrasting case 2 waters and their influence on remote sensing algorithms. *Continental Shelf Research*, 23, 237–250.

Gilerson, A., Zhou, J., Hlaing, S., Schalles, J., Gross, B., Moshary, F., et al. (2007). Fluorescence component in the reflectance spectra from coastal waters—Dependence on water composition. *Optics Express*, 15, 15702–15721.

Gons, H. J., Auer, M. T., & Effler, S. W. (2008). Meris satellite chlorophyll mapping of oligotrophic and eutrophic waters in the Laurentian Great Lakes. *Remote Sensing of Environment*, 112, 4098–4106.

Gons, H. J. (1999). Optical teledetection of chlorophyll-a in turbid inland waters. *Environmental Science & Technology*, 33(7), 1127–1132.

Gons, H. J., Rijkeboer, M., & Ruddick, K. G. (2002). A chlorophyll-retrieval algorithm for satellite imagery (Medium Resolution Imaging Spectrometer) of inland and coastal waters. *Journal of Plankton Research*, 24, 947–951.

Gordon, H. R., Brown, O. B., & Jacobs, M. M. (1975). Computed relationships between the inherent and apparent optical properties of a flat, homogeneous ocean. *Applied Optics*, 14, 417–427.

Jerlov, N. G. (1968). *Optical oceanography.* New York: Elsevier.

Kiefer, D. A., & Reynolds, R. A. (1992). Advances in understanding phytoplankton fluorescence and photosynthesis. In P. G. Falkowsky, & A. D. Woodhead (Eds.), *Primary productivity and biogeochemical cycles in the sea* (pp. 155–174). : Plenum Press.

Kirk, J. T. O. (1984). Dependence of relationships between inherent and apparent optical properties of water on solar altitude. *Limnology and Oceanography*, 29, 350–356.

Kutser, T., Hiire, M., Metsamaa, L., Vahtmae, E., Paavel, B., & Aps, R. (2009). Field measurements of spectral backscattering coefficient of the Baltic Sea and boreal lakes. *Boreal Environment Research*, 14, 305–312.

Le, C., Li, Y., Zha, Y., Sun, D., Huang, C., & Lu, H. (2009). A four-band semi-analytical model for estimating chlorophyll a in highly turbid lakes: The case of Taihu Lake, China. *Remote Sensing of Environment*, 113, 1175–1182.

Magnuson, A., Hardings, L. W., Jr., Mallonee, M. E., & Adolf, J. E. (2004). Bio-optical model for Chesapeake Bay and the Middle Atlantic Bay. *Estuarine Coastal and Shelf Sciences*, 61, 403–424.

Maritorena, S., Siegel, D. A., & Peterson, A. R. (2002). Optimization of a semianalytical ocean color model for global-scale applications. *Applied Optics*, 41, 2705–2714.

Miller, R. L., Belz, M., Castillo, C. D., & Trzaska, R. (2002). Determining CDOM absorption spectra in diverse coastal environments using a multiple pathlength, liquid core waveguide system. *Continental Shelf Research*, 22, 1301–1310.

Mobley, C. D. (1994). *Light and water—Radiative transfer in natural waters.* San Diago: Academic Press (Chapter 5).

Mobley, C. D. (1999). Estimation of the remote-sensing reflectance from above-surface measurements. *Applied Optics*, 38, 7442–7455.

Mobley, C. D., & Sundman, L. K. (2001). *Hydrolight*, 4.2, : Sequoia Scientific, Inc.

Morel, A., & Gentili, B. (1996). Diffuse reflectance of oceanic waters. Remote-sensing problem. *Applied Optics*, 35, 4850–4862.

Morel, A., & Prieur, L. (1977). Analysis of variations in ocean color. *Limnology and Oceanography*, 22(4), 709–722.

Moses, W. J., Gitelson, A. A., Berdnikov, S., & Povazhnyy, V. (2009). Satellite estimation of chlorophyll-a concentration using the red and NIR bands of MERIS—The Azov Sea case study. *IEEE Geoscience and Remote Sensing Letters*, 6(4), 845–849.

O'Reilly, J., Maritorena, S., Mitchell, B., Siegel, D., Carder, K., Garver, S., et al. (1998). Ocean color chlorophyll algorithms for Sea-WiFS. *Journal of Geophysical Research*, 24 937–24 953.

O'Reilly, J., Maritorena, S., O'Brien, M. C., Siegel, D., Toole, D., Menzies, D., et al. (2000). SeaWiFS postlaunch calibration and validation analyses, Part 3. Greenbelt, MD: NASA Goddard Space Flight Center NASA Tech. Memo. 2000–206892, 11.

Pope, R., & Fry, E. (1997). Absorption spectrum (380–700 nm) of pure waters: II. Integrating cavity measurements. *Applied Optics*, 36, 8710–8723.

Simis, S. G. H. (2006). Blue-Green Catastrophe: remote sensing of mass viral lysis of cyanobacteria, PhD dissertation, Vriji University, Amsterdam.

Tzortziou, M., Subramaniam, A., Herman, J. R., Gallegos, C. L., Neale, P. J., & Harding, L. W., Jr. (2007). Remote sensing reflectance and inherent optical properties in the mid Chesapeake Bay. *Estuarine Coastal and Shelf Science*, 72, 16–32.

Werdell, P. J., & Baily, S. W. (2005). An improved In situ bio-optical data set for ocean color algorithm development and satellite data product validation. *Remote Sensing of Environment*, 98, 122–140.